

OPEN ACCESS

# Analysis of Kinetic and Ohmic Resistances in PEM Water Electrolysis through Reference Electrode Measurements

To cite this article: Lena V. Böhre *et al* 2024 *J. Electrochem. Soc.* **171** 054518

View the [article online](#) for updates and enhancements.

## You may also like

- [The Effect of Cell Compression and Cathode Pressure on Hydrogen Crossover in PEM Water Electrolysis](#)  
Agate Martin, Patrick Trinke, Markus Stähler *et al.*
- [\(Invited\) Lowering the Noble Metal Requirement for PEM Water Electrolysis: Membrane Electrode Assembly and Porous Transport Layer Design Considerations](#)  
Maximilian Bernt, Matthias Felix Ernst, Hubert A. Gasteiger *et al.*
- [A brief introduction of electrode fabrication for proton exchange membrane water electrolyzers](#)  
Xinlong Lin, Justin Zhu Yeow Seow and Zhichuan J Xu

## Your Lab in a Box!

The PAT-Tester-i-16: All you need for Battery Material Testing.

- ✓ **All-in-One Solution with Integrated Temperature Chamber (10-80°C)!**  
No additional devices are required to measure at a stable ambient temperature.
- ✓ **Fully featured Multichannel Potentiostat / Galvanostat / EIS!**  
Up to sixteen independent battery test channels, no multiplexing.
- ✓ **Ideally suited for High-Precision Coulometry!**  
Measure with excellent accuracy and signal-to-noise ratio at the same time.
- ✓ **Small Footprint, Easy to Setup and Operate!**  
Cableless connection of 3-electrode battery test cells. Full multi-user, multi-device control via LAN.

 **EL-CELL**<sup>®</sup>  
electrochemical test equipment



Learn more on our product website:



Download the Data Sheet (PDF):



Or contact us directly:

 +49 40 79012-734

 [sales@el-cell.com](mailto:sales@el-cell.com)

 [www.el-cell.com](http://www.el-cell.com)



# Analysis of Kinetic and Ohmic Resistances in PEM Water Electrolysis through Reference Electrode Measurements

Lena V. Bühre,<sup>1</sup> Mustafa Murali,<sup>1</sup> Patrick Trinke,<sup>1</sup> Jonathan Brandt,<sup>1</sup> Debora Brinker,<sup>2</sup> Gözde Kardeş,<sup>2</sup> André Weber,<sup>2</sup> Boris Bensmann,<sup>1,z</sup> and Richard Hanke-Rauschenbach<sup>1</sup>

<sup>1</sup>Leibniz University Hannover, Institute of Electric Power Systems, 30167 Hannover, Germany

<sup>2</sup>Karlsruher Institut für Technologie (KIT), Institut für Angewandte Materialien—Elektrochemische Technologien (IAM-ET), 76131 Karlsruhe, Germany

We investigated a three electrode setup utilized in a temperature variation study to extract the activation energy for the half-cell reactions in PEM water electrolysis and the contributions of electronic resistances to ohmic resistance. The reference electrode configuration used in this investigation is an improved version of a setup previously introduced by our group. Enhancements have been made to minimize the influence of the reference electrode and improve the accuracy of electrochemical impedance spectroscopy.

© 2024 The Author(s). Published on behalf of The Electrochemical Society by IOP Publishing Limited. This is an open access article distributed under the terms of the Creative Commons Attribution 4.0 License (CC BY, <http://creativecommons.org/licenses/by/4.0/>), which permits unrestricted reuse of the work in any medium, provided the original work is properly cited. [DOI: 10.1149/1945-7111/ad4b5d]



Manuscript submitted March 5, 2024; revised manuscript received April 29, 2024. Published May 29, 2024.

Supplementary material for this article is available [online](#)

## List of Abbreviations and Symbols

### Abbreviations

PEMWE	proton exchange membrane water electrolysis
RE	reference electrodes
PEMFC	proton exchange membrane fuel cell
EIS	electrochemical impedance spectroscopy
HFR	high-frequency resistance
SHE	standard hydrogen electrode
CL	catalyst layer
SBRE	salt bridge reference electrode
CCM	catalyst-coated membrane
OER	oxygen evolution reaction
HER	hydrogen evolution reaction
PTL	porous transport layer
GDL	gas diffusion layer
MTX	mass transport and other
MRDE	modified rotating disk electrode
LJP	liquid junction potential
CI	confidence interval

### Symbols

$E$	Nernst potential, V
$T$	temperature, K
$R$	ideal gas constant, 8.3145 J mol <sup>-1</sup> K <sup>-1</sup>
$F$	Faraday's constant, 96485 As mol <sup>-1</sup>
$\eta$	overpotential, V
$U$	voltage, V
$i$	geometric current density, A cm <sup>-2</sup>
$R_{el}$	electronic resistance, $\Omega$ cm <sup>2</sup>
$R_{H+}$	protonic resistance, $\Omega$ cm <sup>2</sup>
$\kappa_0$	reference ionic membrane conductivity, S cm <sup>-2</sup>
$\delta$	thickness, m
$\alpha$	charge transfer coefficients
$i_0$	geometric exchange current density
$E_A$	activation energy
$b$	Tafel slope, mV dec <sup>-1</sup>

### Indices

A	anodic
---	--------

C	cathodic
mem	membrane
Ref	reference
$e^-$	electronic
$\Omega$	ohmic
act	activation/kinetic
mtX	mass transport and other
ptlcl	contact between PTL and CL
f	forward
b	backward

Hydrogen production through electrolysis holds considerable promise for facilitating a decarbonized economy, although concerted efforts are requisite to mitigate associated costs.<sup>1</sup> The medium-term cost reduction is facilitated by enhanced efficiency, prolonged operational lifetimes, and minimized capital expenditures.<sup>2</sup>

To address cost, degradation, and voltage losses attributable to kinetics, exhaustive investigations into catalyst materials and supported catalyst systems have been ongoing over the past decade. Diverse catalysts for the oxygen evolution reaction (OER) at the anode, including iridium black and oxides, iridium-ruthenium combinations, doped iridium oxides, supported iridium-based catalysts, ruthenium catalysts, and noble metal-free materials, have been scrutinized.<sup>3</sup> For the hydrogen evolution reaction (HER) at the cathode, platinum in varied structures such as core-shell types, alloying strategies with Pt involving Ru, Cu, Pd, Ni, and non-platinum group metals have been subject to comprehensive research.<sup>1</sup>

Benchmarking the activity involves comparing parameters such as the activation energy of the electrode reactions. Previous studies have explored OER activation energy for various overpotentials in proton exchange membrane (PEM) fuel cells (PEMFC) and water electrolyzers (PEMWE), neglecting the hydrogen reaction due to its minor contribution to the kinetic overpotential.<sup>4,5</sup> This study analyzes the activation energy for both oxygen evolution reaction and hydrogen evolution reaction at zero overpotential in a technical cell through a reference electrode setup.

In PEMWE, reference electrodes (REs) are utilized to measure the protonic potential within the system. This allows for an improved loss breakdown, enabling the attribution of measured overpotentials to their sources.<sup>6</sup> Various RE configurations have been reported in the literature, such as embedding a reversible hydrogen electrode (RHE) within the membrane, positioning an RHE on the membrane

<sup>z</sup>E-mail: [boris.bensmann@ifes.uni-hannover.de](mailto:boris.bensmann@ifes.uni-hannover.de)

outside of the active area, or establishing a connection between an external RE to the potential of the membrane or catalyst layer.<sup>7–10</sup> This study investigates the latter approach. The RE measurement enables kinetic analysis of both electrodes separately, as presented in an earlier study by this group.<sup>11</sup>

The activation energy can be accessed through a variation of the cell temperature. This parameter proves advantageous not only in the context of catalyst layer development, as previously highlighted, but also holds significance in the modeling of PEMWE cells.

In addition to kinetic losses, this work also delves into ohmic losses. The ohmic resistance of a cell is primarily dictated by ionic resistance and ionomer conductivity, with the contact resistance between the porous transport layer (PTL) and catalyst layer (CL) also playing a role.<sup>12</sup> The reference electrode setup is extended to encompass electrochemical impedance spectroscopy (EIS) measurements, enabling analysis that distinguishes between anodic and cathodic contributions. Subsequently, the temperature variation study is employed to dissect these contributions further, distinguishing between non-temperature-dependent and temperature-dependent factors.

The paper is structured as follows. Initially, the reference electrode setup is illustrated, accompanied by the presentation of equations leading to the kinetic and ohmic analysis. The experimental configuration, previously introduced by this research group,<sup>11</sup> undergoes some refinements, detailed at the outset of the results section. Following this, the discussion proceeds to the outcomes of the temperature variation study, commencing with delineating losses into anodic and cathodic contributions through reference electrode measurements. Subsequently, attention is directed toward the EIS results and the concomitant high-frequency resistance (HFR) analysis. Finally, the paper concludes with an in-depth examination of the kinetic overpotentials.

## Reference Electrode: Materials and Methods/Experimental

**Material and cell setup.**—The laboratory test cell has an active area of 4 cm<sup>2</sup>, featuring gold-coated titanium end plates and flow fields. The reference electrode is introduced into the cell through a small aperture in one of the electrode blocks. For a comprehensive description of the adapted cell, please refer to the details provided in Ref. 11

This study employs commercial catalyst-coated membranes (CCMs) with high loading (Nafion™ N115, 1 mg cm<sup>-2</sup> Pt/C, 2 mg cm<sup>-2</sup> Ir, HIAT gGmbH). Sintered titanium fiber porous transport layers with a thickness of 0.2 mm (2GDL40 Bekaert) are used on the anode, while the cathode utilizes carbon with hydrophobic treatment (E20H, Freudenberg SE). The assembly of the cell is conducted in a wet state. The CCMs, as received from the manufacturer, undergo immersion in deionized water for two hours at room temperature to ensure thorough humidification.

The preparation of PTLs involves washing the titanium PTLs in deionized water using an ultrasonic bath for 15 min at room temperature. Subsequently, an impregnation process is employed to establish an ionic connection through the PTL from the catalyst layer on one side to the salt bridge on the side facing the flow field. Nafion™ solution is utilized for this impregnation, with the precise location of the impregnated spot on the PTL ensured by a mask produced in-house through additive manufacturing. A technical drawing of the mask can be found in Fig. S1 in the supplemental information. The study explores various volumes and concentrations for impregnation, encompassing 1, 1.5, 2.5, and 3.5 μl volumes and concentrations of 5 and 20 wt% Nafion™ solution. The selected impregnation for the remainder of the study is determined as 1 μl of 5 wt% solution.

The salt bridge, integral to the experimental setup, comprises a Nafion™ tube within a Teflon tube and undergoes overnight humidification with deionized water prior to testing. An Ag/AgCl reference electrode from BASi with a 3 mol l<sup>-1</sup> NaCl solution, exhibiting a potential vs standard hydrogen electrode (SHE) at

298.15 K (25 °C) of 196 mV, is utilized as external reference electrode. It is situated in a diluted sulfuric acid solution with a concentration of 0.5 mol l<sup>-1</sup> alongside the end of the salt bridge. Finally, the compression force applied after thermal cell conditioning is set at 3 kN.

**Testing periphery.**—Two different test benches are used to conduct the experiments. The majority of the experiments is performed using the commercial E40 test station from Greenlight Innovation, featuring automated regulation of the anode inlet water temperature and a constant flow rate set at 80 ml min<sup>-1</sup> (anode only). Temperature monitoring is implemented at the cell inlet and the cell outlet in the anode water line. The temperature reported in this manuscript refers to the temperature at the cell inlet. A minor temperature drop is observed between the inlet and outlet, with the magnitude being less pronounced at setpoint temperatures closer to room temperature. The SP150 with a 20 A Booster from BioLogic serves as a potentiostat for all measurements conducted at this test station.

The exemplary half-cell EIS measurements are conducted at the high-pressure PEM water electrolysis test bench, developed and manufactured by the Institute for Applied Materials—Electrochemical Technologies at Karlsruhe Institute of Technology, employing a Zahner Zennium potentiostat.

**Measurement protocol.**—The conditioning process comprises a 0.5 h unpolarized period at the operating temperature. This ensures that the membrane is humidified and that steady-state temperature conditions are maintained. Subsequently, a run-in protocol and polarization measurements are conducted under ambient pressure conditions. The run-in protocol is designed to condition the CCM, while the polarization measurement is intended to assess the cell's properties. The protocols used in each of the two studies in this work are subsequently described.

For the impregnation study, the protocol is outlined as follows: The run-in protocol is a constant current hold at 100 mA cm<sup>-2</sup> for 30 min. The polarization behavior is assessed through a galvanostatic step profile with current steps ranging from 0.001 to 4 A cm<sup>-2</sup>, applied for 10 sec, coupled with impedance measurements (from 100 kHz to 0.1 kHz) at each current density step for the determination of high-frequency resistance. This procedure is repeated twice, amounting to three cycles in total. The concluding cycle is designated for subsequent analysis. Each impregnation process is duplicated.

The temperature variation study follows a slightly different protocol: Polarization behavior is examined using a galvanostatic step profile featuring current steps spanning from 0.006 to 4 A cm<sup>-2</sup>, applied for 10 sec. Impedance measurements are conducted at every current density step to ascertain high-frequency resistance. Similar to the impregnation study, this process is replicated twice, totaling three cycles. Additionally, after each temperature adjustment (from 353.15 K (80 °C) to 303.15 K (30 °C) in 10 K increments), a 1.5 h hold at 100 mA cm<sup>-2</sup> is implemented to ensure a steady state. In the context of the temperature variation study, a run-in protocol is employed, consisting of a complete repetition of the measurement encompassing all temperature steps. The complete measurement is duplicated.

**Data analysis.**—In the following section, we provide an elucidation of the measured voltages and electrochemical impedance spectra. Subsequently, we detail the analysis of loss breakdown, and finally, we present the calculation of the parameters activation energy and ionic conductivity through fitting over temperature.

The measured full cell voltage encompasses the reversible cell voltage and various voltage loss terms. These include proton transport resistance in the membrane and in the anode and cathode catalyst layers, electronic resistance of cell components, and contact resistance between them, kinetic losses, and mass transport losses. The salt bridge reference electrode (SBRE) allows access to the

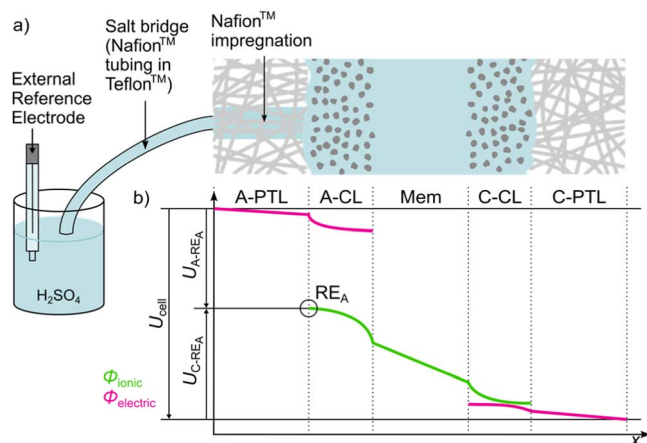


**Figure 1.** Schematic of a typical 5-layer PEMWE cell with salt bridge setup and corresponding exemplary potential distribution for ionic and electronic potentials.

catalyst layer proton potential at the anode electrode. A schematic illustration of a typical 5-layer PEMWE cell and the corresponding exemplary potential distribution of electronic and protonic potentials are depicted in Fig. 1. The electronic potential is at its minimum value on the cathode side and increases along the cell due to electron resistances across different layers. Within the CLs, the difference between ionic and electronic potentials is influenced by the equilibrium potential of the half-cell reactions and kinetic overpotentials. The ionic potential also increases along the cell, influenced by proton transport resistances.<sup>11</sup> Figure 1 visually aids in understanding the potential sensed by the reference electrode, resulting in the voltages:

$$U_{A-RE_A} = E^A + \eta_{act}^A + \eta_{mtx}^A + i \cdot R_{A-RE} \quad [1]$$

$$U_{C-RE_A} = E^C + \eta_{act}^C - \eta_{mtx}^C - i \cdot R_{C-RE} \quad [2]$$

The RE to anode voltage ( $U_{A-RE}$ ) (Eq. 1) includes the OER half-cell Nernst potential ( $E^A$ ), anode activation overpotential ( $\eta_{act}^A$ ), ohmic losses as a function of resistance between the reference electrode and the anode ( $R_{A-RE}$ ), and mass transport and other loss ( $\eta_{mtx}^A$ ). The cell current density is  $i$ . For RE to cathode ( $U_{C-RE}$ ) (Eq. 2), the voltage includes HER half-cell Nernst potential ( $E^C$ ), cathode activation overpotential ( $\eta_{act}^C$ ), ohmic losses as a function of resistance between the cathode and reference electrode, including the entire membrane resistance, ( $R_{C-RE}$ ), and mass transport and other loss ( $\eta_{mtx}^C$ ). Additional explanation on the equations and the potential distribution depicted in Fig. 1 is available in earlier publications of this group.<sup>6,11</sup>

Besides measuring the voltages, electrochemical impedance spectroscopy can measure the high frequency resistance. This measurement gives the full cell HFR and the half-cell values  $R_{A-RE}$  and  $R_{C-RE}$ :

$$R_{A-RE} = R_{el}^{ptl,A} + R_{el}^{ptl,cl,A} + R_{el}^{cl,A} \quad [3]$$

$R_{el}^{ptl,A}$  is the PTL electronic resistance,  $R_{el}^{ptl,cl,A}$  is the contact resistance between anode CL to PTL, and  $R_{el}^{cl,A}$  is the electronic resistance in anodic CL.

$$R_{C-RE} = R_{H+}^{cl,A} + R_{H+}^{mem} + R_{H+}^{cl,C} + R_{el}^{cl,C} + R_{el}^{ptl,cl,C} + R_{el}^{ptl,C} \quad [4]$$

$R_{el}^{ptl,cl,C}$  is the contact resistance cathode CL to PTL,  $R_{el}^{ptl,C}$  is the PTL electronic resistance, and  $R_{H+}^{mem}$  is the ionic resistance in the membrane. Including parts of ionic and electronic resistances within catalyst layers ( $R_{el}^{cl,A}$ ,  $R_{el}^{cl,C}$ ,  $R_{H+}^{cl,A}$ ,  $R_{H+}^{cl,C}$ ) in the HFR remains

debatable. It is pertinent to acknowledge that certain components of the catalyst layer resistance are not represented in the HFR. These resistances can be measured with a non-faradaic transition line approach, which is outside the scope of this work.<sup>13</sup> It is imperative to emphasize that in this work, only the part of electronic and protonic resistance manifesting in the HFR are considered in  $R_{H+}^{cl}$  and  $R_{el}^{cl}$ . In an earlier publication from this group, the electronic resistances in anodic CL were accounted for in the signal from the reference to the cathode. Recent analysis suggests that this resistance is included in the signal from the reference to the anode. An in-depth analysis can be found in Fig. S2 in the supplementary information.

The half-cell HFR values are used to calculate the corresponding ohmic losses:

$$\eta_{\Omega}^{A-RE} = i \cdot R_{A-RE} \quad [5]$$

$$\eta_{\Omega}^{C-RE} = i \cdot R_{C-RE} \quad [6]$$

The resistance  $R_{A-RE}$  is predominantly of electronic origin and exhibits minimal temperature dependence. The temperature coefficient for titanium falls within the range of  $10^{-3} \text{ K}^{-1}$ .<sup>14</sup> The resistance  $R_{C-RE}$  includes both protonic and electronic contributions. Notably, the ionic conductivity of the ionomer demonstrates a pronounced temperature dependence.<sup>15</sup> This temperature dependence (see Eq. 7) has been harnessed in previous studies to deconstruct the high-frequency resistance into distinct components, including membrane resistance, interface resistance, and setup resistance.<sup>12</sup> The  $R_{C-RE}$  can thus be described as:

$$R_{C-RE}(T) = \frac{\delta_{mem}}{\kappa_0} \frac{-E_K}{e^{R \cdot T_{mem}}} + \sum R^{e-} \quad [7]$$

Where  $\kappa_0$  represents reference ionic membrane conductivity for the limit as  $T_{mem}$  goes to infinity,  $\delta_{mem}$  the swollen membrane thickness at operating conditions,  $R$  represents the ideal gas constant, and  $T_{mem}$  is the average membrane temperature. The activation energy for proton transport through the membrane in literature is  $E_K = 7.829 \text{ kJ mol}^{-1}$ .<sup>16</sup>

The calculation of kinetic overpotentials involves utilizing the voltages and ohmic losses. By subtracting the temperature-dependent Nernst potentials and ohmic resistances from the measured voltages expressed in Eqs. 1 and 2, the resultant contributions comprise kinetic overpotentials and other factors such as mass transport and other losses. Neglecting mass transport and other losses for small current densities below  $0.1 \text{ A cm}^{-2}$  is customary. A linear approach is employed for the fast hydrogen evolution reaction in the current density range below  $0.1 \text{ A cm}^{-2}$ :

$$\eta_{act}^{HER} = \frac{i}{i_0^{HER}} \frac{RT}{F(\alpha_f + \alpha_b)} \quad [8]$$

Where  $F$  is the Faraday constant. The summation of charge transfer coefficients ( $\alpha$ ) is presumed to be equal to 1. This assumption aligns with common practice in literature where many reactions tend to be symmetrical. In the absence of specific information, it is generally accepted to consider both charge transfer coefficients as 0.5.<sup>17</sup> The slope in this context corresponds to the exchange current density ( $i_0$ ). The theoretically anticipated intercept with the y-axis is zero; however, an offset was observed in certain instances. This offset corresponds to a potential shift from the salt bridge, which is discussed in detail in the results section. Subsequently, this observed shift was corrected in the half-cell voltages. This procedure was used in another work where a shift in the reference electrode potential occurred.<sup>9</sup>

For the sluggish OER, a Tafel fitting in the range of  $0.01$ – $0.1 \text{ A cm}^{-2}$  is employed, where  $b$  represents the Tafel slope:

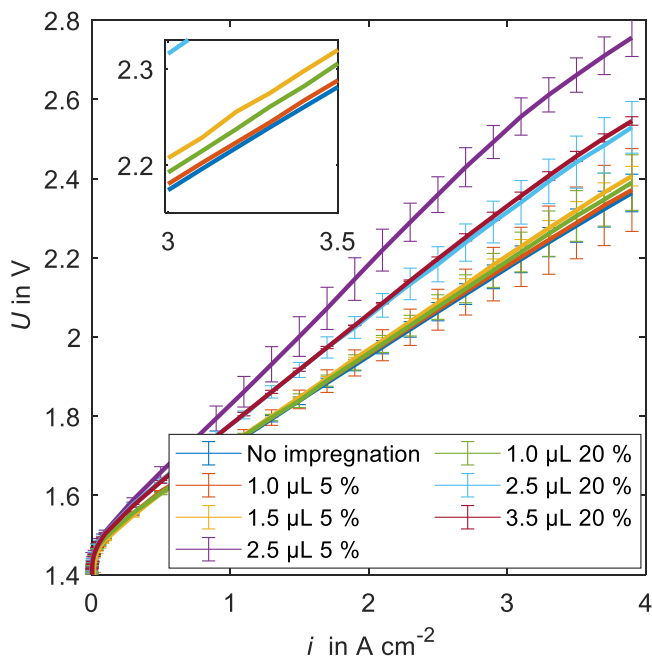


**Figure 2.** Cell polarization curve for non-impregnated PTLs and for PTLs with different impregnation volumes in combination with different mass fractions (5 and 20 wt%) of Nafion™ solution at 333.15 K (60 °C). The inset provides a zoomed-in view of the “No impregnation” curve and its adjacent curves at higher current densities. Error bars are omitted in the inset for clarity.

$$\eta_{\text{act}}^{\text{OER}} = b \cdot \log \frac{i}{i_0^{\text{OER}}} \quad [9]$$

For both OER and HER, the determination of the exchange current density is derived through kinetic analysis. In the final step of this analysis, the temperature dependence of the exchange current density is employed to gain insights into the activation energy at zero overpotential. The temperature dependence of the exchange current density for the OER and HER can be expressed with the Arrhenius equation:<sup>12</sup>

$$i_0^{\text{OER}} = i_0^{\infty, \text{OER}} \cdot e^{-\frac{E_A^{\text{OER}}}{RT}} \quad [10]$$

$$i_0^{\text{HER}} = i_0^{\infty, \text{HER}} \cdot e^{-\frac{E_A^{\text{HER}}}{RT}} \quad [11]$$

Where  $E_A$ , is the activation energy and  $i_0^{\infty}$  is the exchange current density at reference state for the limiting case as T approaches infinity.

## Results and Discussion

The first part of the results involves an examination of enhancements and discussions pertaining to the experimental setup, as compared to the configuration detailed in Ref. 11. This examination encompasses the determination of the optimal quantity of ionomer for the impregnated PTLs, an investigation into concentration differences over the salt bridge, and exploration of half-cell EIS measurements.

Subsequently, the focus shifts to the presentation and utilization of the dataset obtained from the temperature variation experiments. Within this context, the HFR is subjected to further dissection, providing deeper insights into its components. Additionally, a detailed analysis of the kinetic overpotential is conducted to probe the HER and OER activation energy.

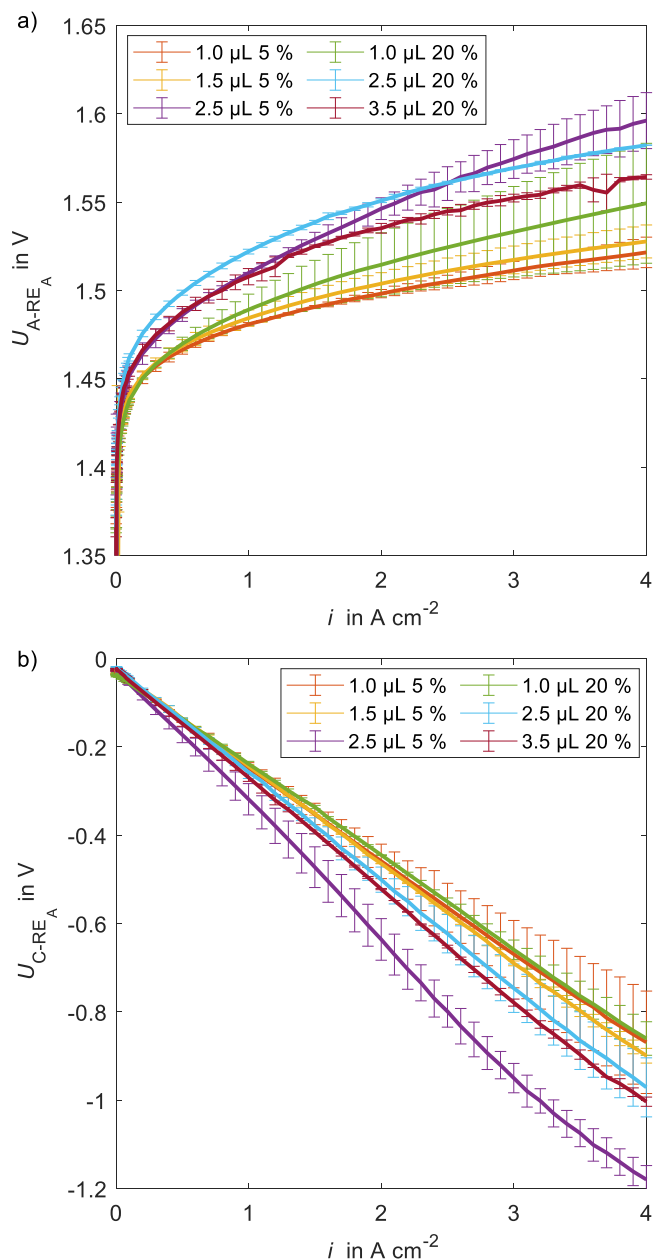


**Figure 3.** Half-cell polarization curve for different impregnation volumes and mass fractions at 333.15 K (60 °C), (a) Anode to  $RE_A$  and (b) Cathode to  $RE_A$ .

**Nafion™ impregnation.**—Initially, the outcomes of the full cell polarization curve are examined for both the pristine PTLs and PTLs subject to various degrees of impregnation. The findings are visually presented in Fig. 2. Notably, a discernible trend emerges where lower impregnation volumes result in cell performance more closely aligned with that of the non-impregnated counterpart. Elevating the impregnation volume to 2.5  $\mu\text{L}$  and beyond induces a significant increase in overpotentials for both mass fractions, with a more pronounced increase observed for the 5 wt% solution. The following observation is made during the material preparation phase prior to the commencement of the experiment. Following the application of the larger volumes to the PTL, a notable local expansion of the impregnated area is observed, suggesting a potential compromise in the performance of significant portions of the active area. However, the reason for the significant deviation of the 5 wt% impregnation remains unclear.

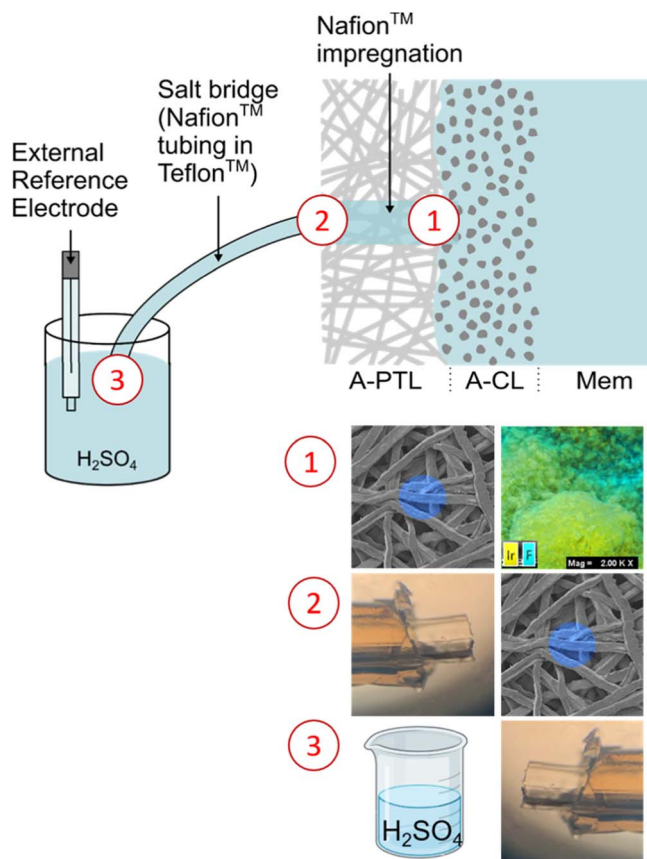


**Figure 4.** Schematic of the experimental setup with RE at the anode. Indication of interfaces of (1) catalyst layer and impregnated PTL, (2) impregnated PTL and solid Nafion<sup>TM</sup> tubing, and (3) solid Nafion<sup>TM</sup> tubing and liquid H<sub>2</sub>SO<sub>4</sub> electrolyte.

Subsequently, impregnation volumes of 1.0  $\mu\text{l}$  and 5% are identified as the closest approximations, warranting their selection for inclusion in the subsequent temperature variation study.

Beyond the primary objective of mitigating the impact of impregnation on cell performance and ideally achieving parity with non-impregnated conditions, a secondary goal emerges concerning the quantity of impregnation. This secondary objective pertains to ensuring the presence of adequate ionic contact to effectively bridge the potential from the CL to the salt bridge.

To assess the adequacy of ionic contact, measurements of half-cell potentials are conducted using the impregnated PTLs from above. The results, depicted in Fig. 3, reveal that sufficient ionic contact is maintained across all impregnation levels. The consistent recording of half-cell potentials evidences this. In scenarios where ionic contact is lacking, irregularities such as substantial jumps in the order of up to 10 V are observed. Furthermore, in cases of no connection at all, the half-cell voltages initiate at the maximum value of the potentiostat. Figure 3 illustrates the steady recording of half-cell potentials across varying impregnation volumes. Notably, larger impregnation volumes are associated with increased losses in the half-cell curves. Both half-cell voltages have the best performance for the impregnation with a 5 wt% Nafion<sup>TM</sup> solution of 1.0  $\mu\text{l}$ .

It is noteworthy that employing lower volumes or mass fractions of Nafion<sup>TM</sup> solution may yield comparable results and offer a viable alternative for impregnation. The material and volume utilized in this study fall within the confines of availability in the laboratory. Given their promising performance, further investigation is not currently being conducted.

**Concentration cell and liquid junction potential of SB setup.**— This subsection provides a detailed analysis of the protonic bridge

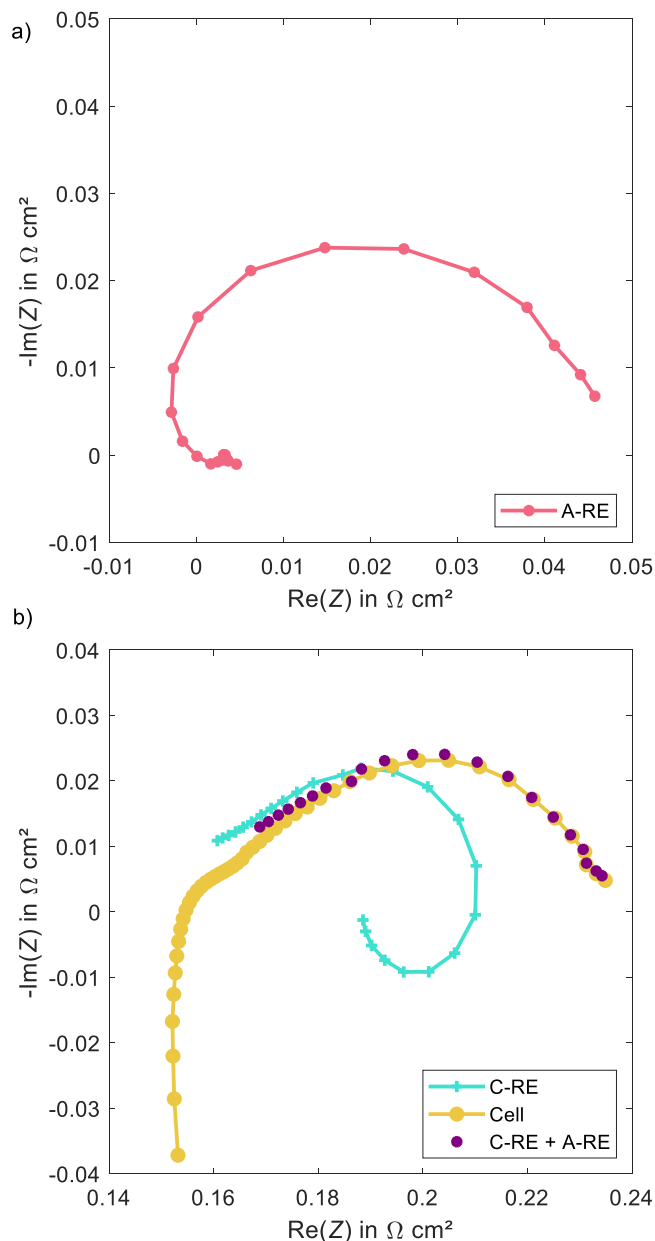


**Figure 5.** Nyquist plot of (a) anode (A-RE), tested at  $0.36 \text{ A cm}^{-2}$  with amplitude of  $0.2 \text{ A cm}^{-2}$  and frequency range from 0.6 kHz to 0.5 Hz, (b) cathode (C-RE), tested at  $0.36 \text{ A cm}^{-2}$  with amplitude of  $0.2 \text{ A cm}^{-2}$  and frequency range from 0.6 kHz to 0.5 Hz, total cell impedance (Cell) tested at  $0.36 \text{ A cm}^{-2}$  with amplitude of  $0.2 \text{ A cm}^{-2}$  and frequency range from 100 kHz to 0.5 Hz and sum of anode and cathode impedance (C-RE+A-RE) (0.6 kHz to 0.5 Hz).

extending from the catalyst layer to the external reference electrode. This bridge involves a pathway through the impregnated PTL and the Nafion<sup>TM</sup> tubing into the liquid H<sub>2</sub>SO<sub>4</sub> solution.

The established protonic pathway involves multiple interfaces, where the concentration of ions plays a pivotal role. The concentration at these interfaces may induce the development of a concentration potential and, potentially, a liquid junction potential. These interfaces are identified as follows, and visual representation can be found in Fig. 4:

1. Ionomer in the catalyst in contact with Nafion<sup>TM</sup> impregnation in the pores of the PTL.
2. Nafion<sup>TM</sup> impregnation in pores of the PTL in contact with Nafion<sup>TM</sup> tubing.

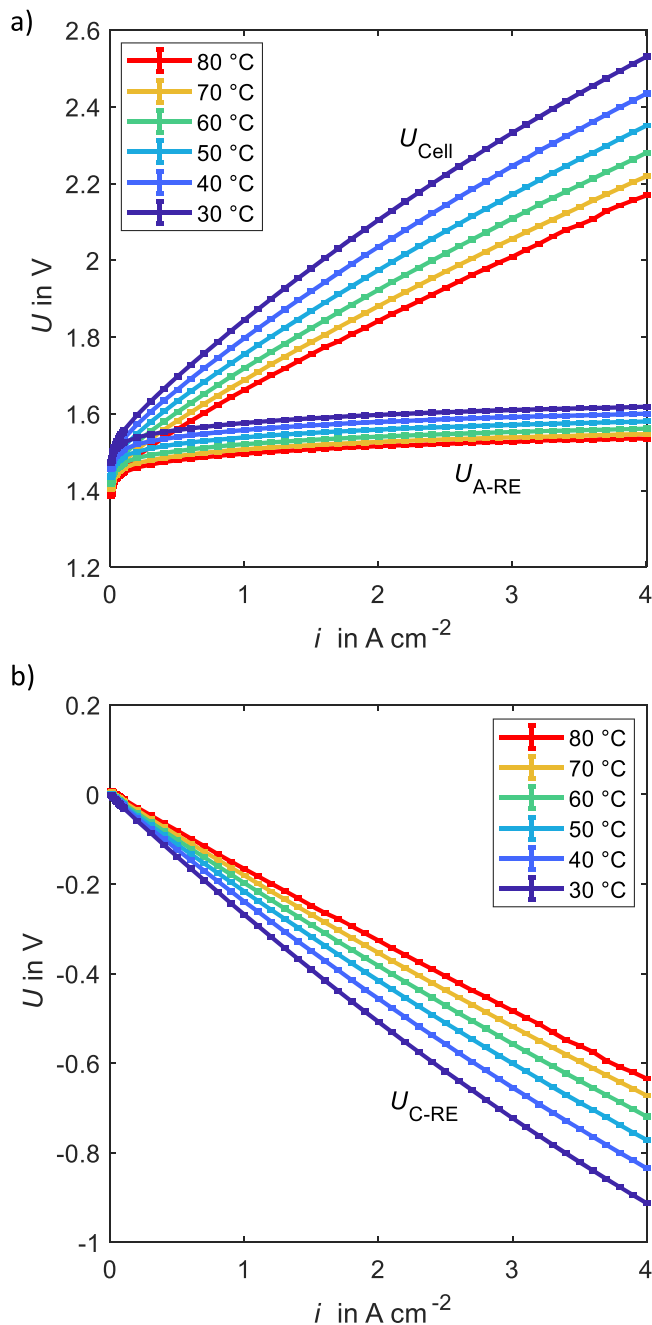


**Figure 6.** Polarization curves of a PEM water electrolysis cell with standard material at 30 °C–80 °C with RE at the anode, for (a) full cell and anode to reference and (b) cathode to reference.

### 3. Nafion™ tubing in contact with H<sub>2</sub>SO<sub>4</sub> solution.

The proton concentration of Nafion™ depends on various factors such as its concentration, equivalent weight, humidification, and temperature.

To underscore the relevance of these interfaces to the reference potential, we observe two key phenomena. First, alterations in the liquid electrolyte concentration by dilution with deionized (DI) water under constant conditions result in an instantaneous shift in half-cell potentials. Second, during the study of impregnation volume, a slight shift in half-cell potentials (order of 15 mV) that correlates with the impregnation volume is observed, emphasizing the importance of studying the concentration potential over the bridge.

Despite the significance, in situ measurements of the concentration potential over the bridge pose challenges. Consequently, we propose an ex situ measurement of isolated interfaces. For instance, the interface between the Nafion™ tubing and the liquid electrolyte can be analyzed using two beakers of liquid electrolyte connected via the tubing, yielding a measured potential smaller than 3 mV (H<sub>2</sub>SO<sub>4</sub>, identical 7.6 mM concentration in both beakers, room temperature, Ag/AgCl RE on both sides). This observation indicates that the interaction between the tip of the salt bridge and the liquid electrolyte plays a minimal role in generating a potential gradient across the bridge.

Further investigation of interfaces towards and from the PTL proves challenging in ex situ experiments. An alternative approach involves estimating potentials using the Nernst equation, contingent upon proton concentration. However, information on the pH of Nafion™ is limited. Literature provides proton concentration values for fully saturated Nafion™, but the diverse structures of Nafion™ in our setup—from the catalyst layer to PTL impregnation to Nafion™ tubing—complicate estimating proton concentrations at the interfaces.<sup>18</sup>

The occurrence of liquid junction potential (LJP) was mentioned in prior works by Becker et al., yet they concluded that its estimation posed considerable challenges.<sup>19</sup> These collective findings underscore that a potential shift in the reference potential should be accounted for in the data analysis.

**EIS for half-cells.**—Subsequently, the investigation deals with the half-cell EIS, a domain not previously explored with this setup. In prior studies, HFR measurements from EIS were exclusively conducted for the full cell, omitting the half-cells due to significant outliers at high frequencies. Recognizing the importance of half-cell HFR values, collaborative efforts with experts in the field were initiated to better understand the resulting spectra.

The outcomes of this effort include enhanced EIS settings, where refined configurations were adopted to circumvent challenges associated with high frequencies and inductivities in the setup. Notably, high frequencies were strategically avoided to mitigate the influence of inductivities, which tended to produce large outliers. Figure 5 presents the Nyquist plots for the anode to reference (A-RE) half-cell in (a) and the cathode to reference (C-RE) half-cell and the full cell in Fig. 5b. The full cell exhibits a zero-axis intercept, yielding the HFR at 10 kΩ. While the C-RE signal has an intercept at the low frequency resistance, it requires fitting to access the HFR. The resulting HFR is marginally lower compared to the full cell HFR. The A-RE in Fig. 5a Nyquist plot is smaller, resulting in a minor HFR from RE to the anode, aligning with expectations. The sum of the half-cell values matches the measured full cell values in Fig. 5b. It is important to emphasize that the frequency range for the A-RE signal imposes a limitation on the frequency range of the calculated sum, resulting in fewer data points for the curve compared to the C-RE and full cell signals. The main focus of the EIS measurement in this study is the HFR. In addition, the following observation deserves a brief discussion. The half-cell Nyquist plots both exhibit loops, the A-RE signal at higher frequencies and the C-RE at lower frequencies, which are not present in the full cell signal. A similar observation is made by Adler for a different RE setup. In his work, the loops at low and high frequencies appear due to different time constants at the electrodes.<sup>20</sup> Similar observations are made for batteries in case of asymmetries and different electrode characteristics.<sup>21,22</sup> Corresponding Kramers Kronig results are detailed in Fig. S3 in the supplementary information.<sup>23–25</sup> It should be noted that the signal for the A-RE values has small values and lies in the limit range of the potentiostat.

Furthermore, additional tests were conducted on the setup using the Zahner Zennium with a system impedance of 10 TΩ. The impedance of the salt bridge was examined by connecting the anode and the reference electrode as the working electrode and counter electrode, respectively. Applying a small AC voltage (20 mV) over the open-circuit voltage yielded a current in the nA range, and the

resulting impedance of 100 k $\Omega$  fell within a minimal range of the system impedance of 10 T $\Omega$ .

**Polarization curves with temperature variation.**—The results for the full cell and half-cell voltages over current density for the different temperatures are presented in Fig. 6. To ensure stationarity, the three repetitions are compared and verified to be identical, and the third cycle is subsequently selected for analysis. Error bars are calculated from the duplicated measurement. As expected, the cell voltage increases as the cell operates at lower temperatures due to increased voltage losses. The dataset will subsequently be employed to analyze parameters related to ohmic resistance and kinetic resistance.

The performance aligns with expectations when compared to literature data featuring similar materials. While the selection of the external Ag/AgCl-RE may have potential implications for contamination by chloride ions from the reference electrode, as noted in a previous publication, no such impact on performance was observed in this study.<sup>11</sup>

**High frequency resistance measurements.**—The HFR is measured for the full cell and the two half-cells in the frequency range of 100 kHz to 0.1 kHz. The intercept frequency for the full cell is around 3 kHz and around 1 kHz for the half-cells. The results as a function of current density are shown in Fig. 7. Notably, for current densities below 0.5 A cm<sup>-2</sup>, extrapolation was necessitated due to the presence of noise in the spectra and inherent imprecision in the HFR calculations. The observed noise within the spectra is a consistent phenomenon not only in the three-electrode setup but also prevalent in standard two-electrode setups. This phenomenon is particularly pronounced when integrating the RE setup into the test station used in our study and may arise due to various factors inherent in the experimental setup. The cables and the test cell contribute to the signal distortion, resulting in mutual inductance effects.

The reported errors in the results are derived from the standard deviation of duplicated measurements. For the cell and cathode to reference HFRs, an overall increase with lower operating tempera-

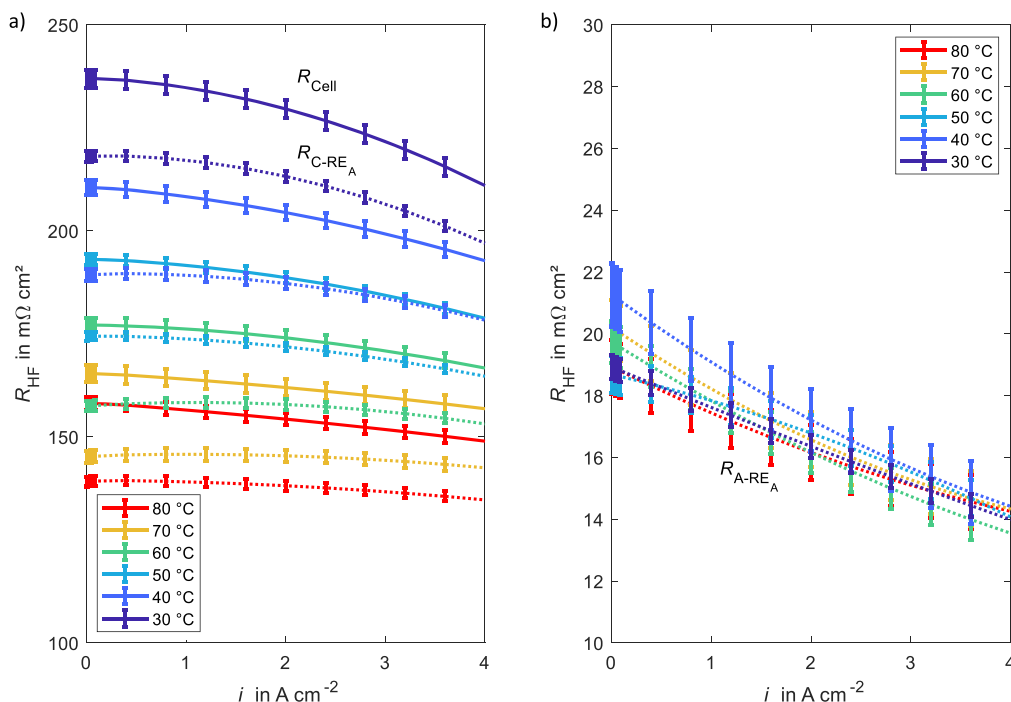


**Figure 7.** HFR values for cell (a), C-RE (a, dashed lines), and A-RE (b) as a function of current density for different temperatures. For clarity, only every fourth measurement point is displayed.

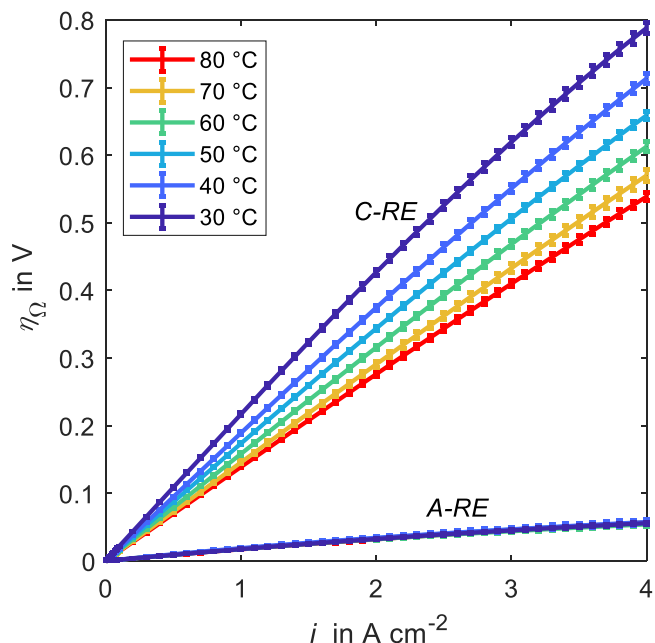


**Figure 8.** Ohmic overpotentials from anode to reference and from cathode to reference over current density for different temperatures.

ture can be observed. The anode to reference HFR exhibits a less defined trend. Moreover, the HFRs show a decreasing trend at higher current density, which is more pronounced at lower operating temperatures. This temperature-dependent influence on the HFR, particularly noticeable for current densities exceeding 1 A cm<sup>-2</sup>, has been previously documented.<sup>12</sup> In this study, the potential amplification of this effect at lower temperatures is conceivable due to the elevated overpotentials, resulting in increased temperature elevation and subsequent enhancement in conductivity. Furthermore, the reduced proton conductivity at lower operating temperatures is



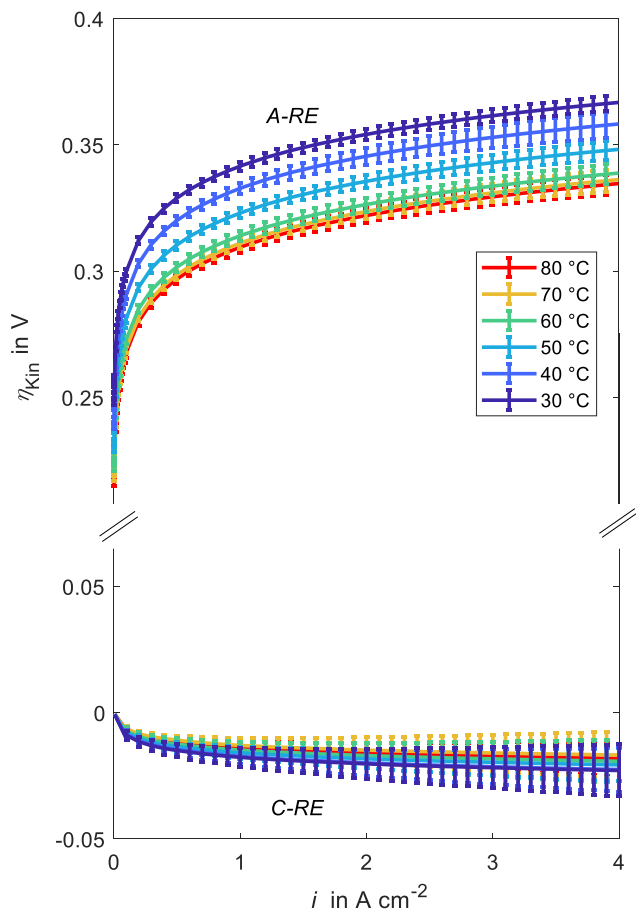


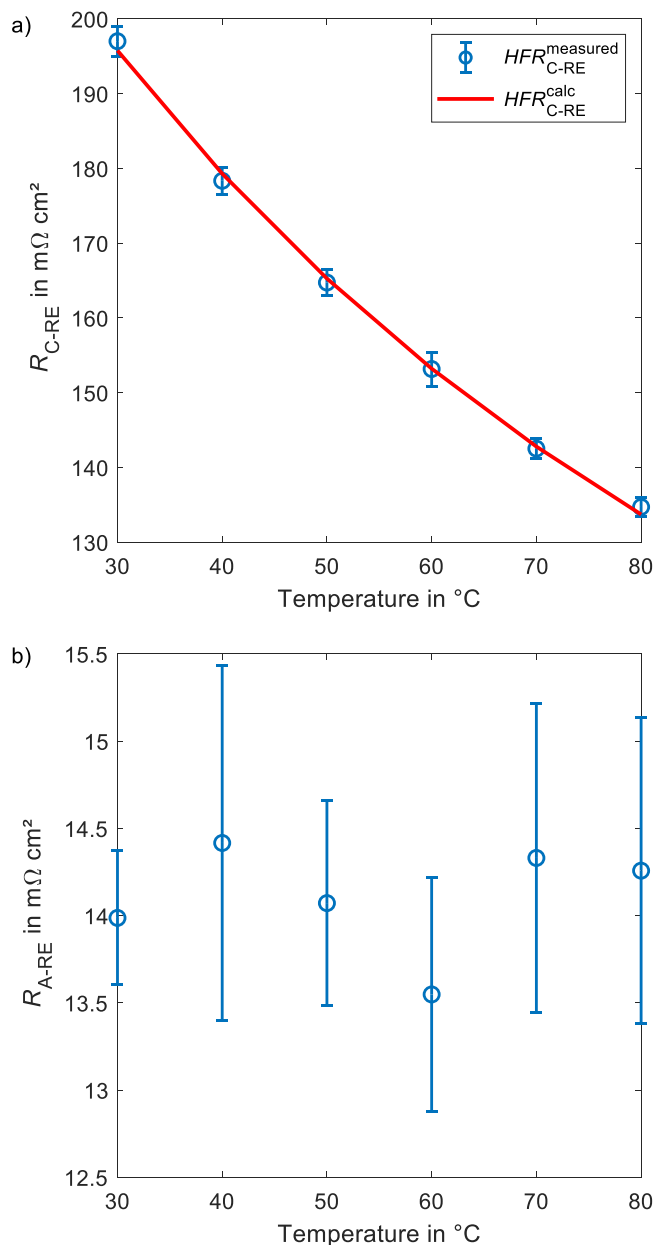
**Figure 9.** Modell-based kinetic overpotentials from (a) anode to reference and from (b) cathode to reference over current density for different temperatures.

anticipated to expedite the movement of the reaction front toward the membrane with higher current density, thereby accentuating the decrease in HFR. These HFR values and the voltage dataset from the preceding subsection constitute integral components for subsequent in-depth data analysis.

**Loss breakdown.**—The voltage dataset, in conjunction with the measured HFR, provides a foundation for dissecting the losses within the cell. As a first step, the ohmic losses are calculated as indicated in Eq. 5. The outcomes are visually presented in Fig. 8. Notably, the ohmic loss from the reference to the cathode surpasses the contribution towards the anode. This aligns with expectations, considering that a significant portion of the ohmic losses emanate from the membrane protonic resistance quantified in the RE-C signal. Consistent with the trends observed in  $HFR_{C-RE}$  values, ohmic losses towards the cathode exhibit an increment with a decrease in operating temperature.

Upon correcting the voltages obtained from Fig. 6 for both ohmic losses and the temperature-dependent Nernst contributions, the resultant values are employed for kinetic analysis. Specifically, the anodic and overall cell contributions are calculated through Tafel fitting (see Eq. 9) at low current densities ( $0.01\text{--}0.1\text{ A cm}^{-2}$ ) and extrapolated to encompass the entire current density range. Simultaneously, the cathodic contribution at low current density is approximated using a linear fitting, as indicated in Eq. 8. However, it is imperative to note that the validity of linear fitting diminishes for larger current densities. Figure 9 visualizes the kinetic losses over current density.

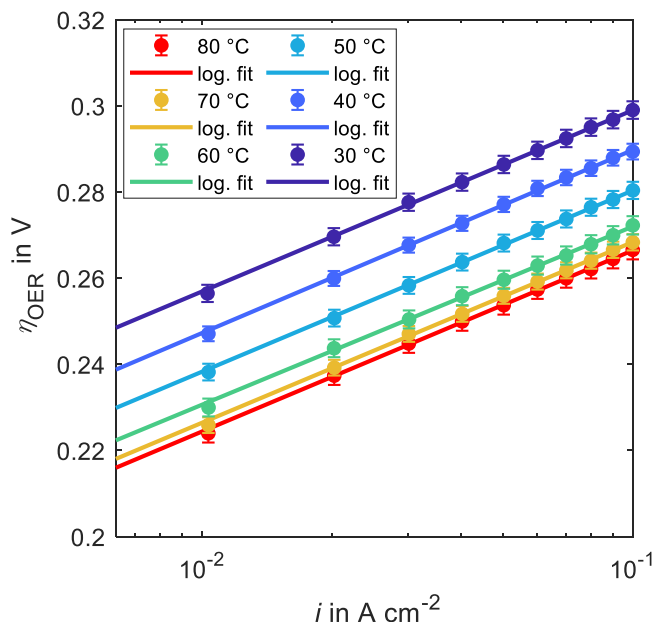
The anodic contribution associated with the oxygen evolution reaction (Fig. 9a) overpasses the cathodic contribution linked to the



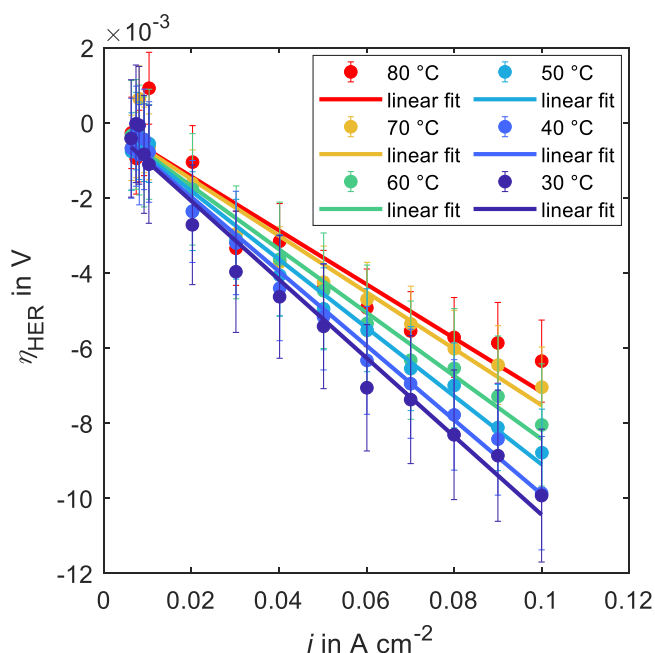
**Figure 10.** HFR at  $4\text{ A cm}^{-2}$  over temperature (a)  $R_{C-RE}$  with the fitting of Eq. 7 and (b)  $R_{A-RE}$ .

hydrogen evolution reaction (Fig. 9b). Both components exhibit an increase with diminishing temperature, aligning with anticipated trends. The cathodic contribution in Fig. 9b) is calculated from linear fitting below  $0.1\text{ A cm}^{-2}$ . Above current densities of  $0.1\text{ A cm}^{-2}$  it is calculated by subtracting the anodic contribution from the total cell kinetic loss. The error is from the error propagation of the cell voltage error and the HFR error. Given the minor magnitude of the HER kinetic losses and the multiplication of the  $HFR_{C-RE}$  error with the current density, it becomes evident that the error amplifies notably at higher current densities.

**Separation of Ohmic resistance via temperature variation.**—Building upon the aforementioned measurement data and loss breakdown, an in-depth examination of temperature dependencies is undertaken, focusing on ohmic losses in this subsection. The temperature variation is leveraged to dissect the losses into components influenced by temperature and those independent of temperature.



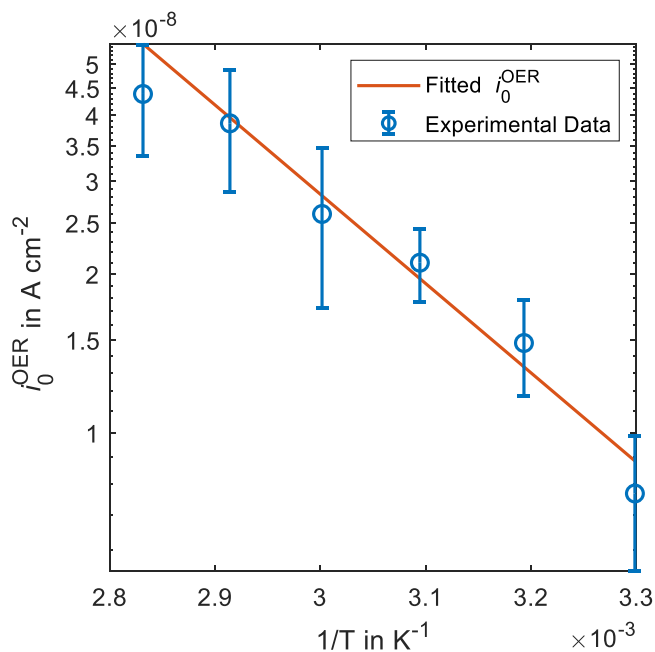
**Figure 11.** OER kinetic overpotential over current density for low current density range. Measurement data and results from Tafel fitting for different temperatures.



**Figure 12.** HER kinetic overpotential over current density for low current density range. Measurement data and results from linear fitting for different temperatures.

For this analysis, we select a current density of  $4 \text{ A cm}^{-2}$ , acknowledging the observed dependence of the HFR on current density in prior sections. This dependence was tentatively attributed to the interplay of temperature increase with larger current. Another influencing factor is a shift of the reaction zone within the catalyst layer. Whether the electrochemical reaction occurs near the membrane or towards the PTL could exert a reciprocal influence on other mechanisms and impact the part of catalyst layer resistances that can be measured in the HFR. The present analysis is confined to this specific current density.

The corresponding HFR values for A-RE and C-RE over the range of the cell inlet temperatures are graphically presented in



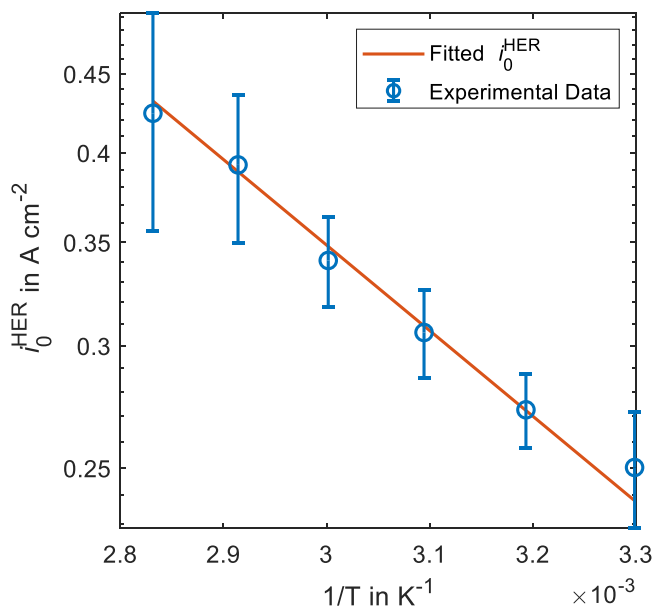
**Figure 13.** Exchange current density of OER over temperature and corresponding fit of Arrhenius equation.

Fig. 10. Error bars in the figure are indicative of repeated measurements. While the anode contribution exhibits no distinct trend with temperature, the cathode contribution unequivocally diminishes as temperature decreases.

In accordance with Eq. 7, the non-temperature dependent part of  $HFR_{C-RE}$  ( $R^{e-}$ ) and the ratio between the swollen membrane thickness and the reference conductivity for infinite  $T_{mem}$  ( $\delta_{mem}/\kappa_o$ ) can be determined by fitting the equation to the measured data. Due to heteroscedasticity, a method of weighted least squares is used. The fitting process employs an optimization approach utilizing the trust-region-reflective algorithm provided by Matlab.<sup>26</sup> The perfect linear relationship between parameters  $\delta_{mem}$  and  $\kappa_o$  in Eq. 7, additionally indicated by a correlation coefficient of one, results in one redundant parameter and causes compensation effects in the optimization process. To address this issue, both parameters are combined into their ratio for the fitting process. Further details about the performed optimization are attached in Table S1 in the supplementary information. The results of the fitting yield, with a coefficient of determination of 0.998:

- $\delta_{mem}/\kappa_o = 7.7 \pm 0.4 \text{ m}\Omega \text{ cm}^2$
- $R^{e-} = 22.7 \pm 6.9 \text{ m}\Omega \text{ cm}^2$

Literature values for the reference ionic membrane conductivity ( $\kappa_o$ ) lie in the range of  $\kappa_o = 2.29 \text{ S cm}^{-1}$ .<sup>15,16</sup> The dry thickness of Nafion™ 115 is  $125 \mu\text{m}$ . Nafion™ swelling is substantial, e.g., an N117 membrane may swell up to 16%–26%,<sup>12</sup> which would correspond for N115 to a swollen thickness of  $145\text{--}157 \mu\text{m}$ . This would result in a ratio of  $6.3\text{--}6.9 \text{ m}\Omega \text{ cm}^2$ . The value calculated here is slightly elevated. A possible reason for the discrepancy may be ascribed to the inclusion of protonic resistance in the catalyst layers in the temperature-dependent HFR. Moreover, the inlet water temperature is used to approximate  $T_{mem}$ . It is important to note that the inlet temperature may not accurately represent the actual membrane temperature. The inlet temperature matches the setpoint temperature and is slightly higher compared to the outlet temperature, particularly at higher setpoint temperatures. This discrepancy is due to the lack of insulation in the cell and outlet water connection. The membrane temperature might, therefore, be lower than the inlet temperature. Conversely, during operation, the membrane temperature tends to rise due to the heat generated by overpotentials.<sup>12</sup>



**Figure 14.** Exchange current density of HER from experimental analysis over temperatures and results from fitting of Arrhenius equation.

Given these conflicting trends, determining the exact membrane temperature proves challenging. If either the reference ionic membrane conductivity or the swollen membrane thickness is known, the other parameter can be estimated. The ratio of both, as calculated here, can be used in modeling.

Notably, the non-temperature-dependent contribution on the cathode ( $R^{e-}$ ) exhibits a slight increase in comparison to the analogous anode values, which have a mean value of  $14.1 \pm 0.7 \text{ m}\Omega \text{ cm}^2$ . Nonetheless, the confidence interval of the cathode contributions encompasses the values obtained from the anode contributions. The values depend on the conductivities of materials (carbon cloths vs titanium fiber), the effective conductivity of the catalysts (platinum on carbon vs iridium/iridium oxide), and the corresponding interface.

**Analysis of activation energies through temperature variation.**—The temperature variation is employed to scrutinize the kinetic losses, utilizing the HFR and Nernst-corrected half-cell voltages. The fitting process adheres to the methodology outlined in Eqs. 8 and 9. A linear fitting approach is adopted for the hydrogen evolution reaction's kinetics. A key parameter of interest is the slope of the linear fitting for HER kinetics which is related to the exchange current density.

Simultaneously, with the corrected OER values, Tafel fitting is executed to determine the Tafel slope and, notably for subsequent analyses, the exchange current density. A comprehensive summary of all fitted results is provided in Table S2 in the supplementary information.

The Tafel fit results for the oxygen evolution reaction kinetics are displayed in Fig. 11 as a semi-logarithmic plot. Elevated temperatures reduce the y-axis intercept, while the slope remains largely unaffected by the temperature. The obtained Tafel slope remains consistent across different temperatures, suggesting that the rate-determining step remains unchanged regardless of temperature variations.

The results of the linear fit for HER kinetics are graphically depicted in Fig. 12. A discernible trend reveals a steeper increase in kinetic losses when operating at lower temperatures. The observed errors stem from the error propagation inherent in the repetitive half-cell measurements and the HFR measurements.

From the conducted fittings, the exchange current density is computed for the half-cell reactions. The exchange current density and temperature serve as input parameters for Eq. 10, aiming to fit

the activation energy. As before, we employed a weighted least squares method coupled with an optimization approach utilizing the trust-region-reflective algorithm. The ensuing results are outlined below, with an initial emphasis on the anodic OER.

Figure 13 illustrates the measurement data of the anodic exchange current density in logarithmic scale over temperature alongside the outcomes derived from fitting Eq. 9. The resultant activation energy is  $E_A^{\text{OER}} = 29.5 \pm 7.8 \text{ kJ mol}^{-1}$ . The exchange current density at reference state (T to infinite) is  $1.1 \pm 3 \text{ mA cm}^{-2}$ . If a different reference temperature is chosen, the exchange current density at reference state will change. The exchange current density at the reference state is useful for modeling purposes but will not be further analyzed here. The coefficient of determination is 0.961. The optimization settings are concisely outlined in Table S3 in the supplementary information.

As previously discussed concerning the fitting of ohmic resistance, it is important to mention the utilization of the cell inlet temperature as an approximation for the reaction temperature. It is worth reiterating that this approximation may lack accuracy due to heat ingress into the system from overpotentials and heat egress from the system into the surrounding environment.

The aperture within the electrode block intended for the salt bridge can alternatively serve as an entry point for inserting a temperature sensor to gauge the internal temperature of the cell.<sup>27</sup> However, it is not yet feasible to accommodate both sensors within this space simultaneously, which restricts temperature measurements to the cell's inlet and outlet points.

A similar study was carried out by Suermann et al. with a temperature variation between 30 and 70 °C for the full cell. Their study obtained an activation energy at zero overpotential of  $65 \pm 10 \text{ kJ mol}^{-1}$ , which they subscribe to the OER.<sup>28</sup> While the exchange current densities in their work generally lie higher compared to the present work, the increase of exchange current densities over temperature is also more pronounced. The difference might be associated with differences in the materials (CCM catalyst material IrO<sub>2</sub> vs Ir black, different loadings) and setup (pressure 10 bar vs ambient).

Kroschel et al. used a modified rotating disk electrode (MRDE) setup in comparison with a full cell to analyze the activation energy of the OER. The MRDE allows for the analysis of CCMs. Temperatures used in their study range from 298.15 K (25 °C) to 343.15 K (70 °C) in steps of 15 K. For the MRDE measurements, the exchange current densities at ambient temperature exhibit a comparable range to those observed for OER within this investigation. The activation energy at zero overpotential is estimated at approximately  $75 \text{ kJ mol}^{-1}$ . However, when employing a test station, a slightly lower value of  $68 \text{ kJ mol}^{-1}$  is obtained. This discrepancy between MRDE and full cell testing is attributed to electrolyte interactions. Similarly to Suermann et al., the contribution from HER was assumed to be negligible in their full cell analysis.<sup>29</sup> The disparate outcomes observed in comparison to those of the present study may be attributed to this assumption and variations in materials, including the selection of catalyst material (CCM with IrO<sub>2</sub> versus Ir black) and differing loadings.

Lettenmeier et al. found activation energies at zero overpotential for Ir-black and a nanostructured iridium catalyst of  $52 \text{ kJ mol}^{-1}$  and  $40 \text{ kJ mol}^{-1}$ . They used an RDE setup and a temperature range from 303.15 K (30 °C) to 242.15 K (70 °C).<sup>30</sup> Although these authors employed a catalyst similar to the one utilized in this study (Ir-black), their experimental setup exhibited notable divergence. Studies have demonstrated that conducting full cell CCM testing, as opposed to RDE or gas diffusion electrode testing, yields disparities in kinetic parameters and their temperature-dependent trends. These differences arise from factors such as variations in catalyst layer utilization.<sup>31</sup>

Schuler et al. determined the activation energy at zero overpotential to be  $42.5 \pm 10 \text{ kJ mol}^{-1}$  for an IrO<sub>2</sub>/TiO<sub>2</sub> catalyst. Their investigation utilized a vapor-fed operation at temperatures of 343.15 K (70 °C) and 353.15 K (80 °C). Notably, their reported value falls within an overlapping confidence interval with our findings.<sup>32</sup>

Published values for the OER activation energy at zero overpotential vary depending on the analytical method and the materials studied. The values reported in this study fall towards the lower end of the spectrum observed in existing literature. This disparity may be attributed to the assumption made regarding the inlet cell temperatures used to fit the Arrhenius equation. At higher cell temperatures, enhanced heat transfer to the environment may lead to a slightly lower membrane temperature. Conversely, at lower temperatures, increased overpotentials and heat production may elevate the membrane temperature. This compression of the temperature window could consequently yield a slightly higher activation energy. Additionally, this study differs from previous approaches by investigating full cell operation without neglecting the HER contribution.

The results for the HER exchange current density are displayed in Fig. 14. The fitting results in an activation energy of  $E_A^{\text{HER}} = 9.9 \pm 1.2 \text{ kJ mol}^{-1}$ . The exchange current density at reference state (T to infinite) is  $11.1 \pm 0.6 \text{ A cm}^{-2}$ . The coefficient of determination is 0.992. The literature lacks comparable values for full cell HER analysis. Comparison with analysis carried out in liquid electrolytes for platinum in an acidic environment resulted in larger values of  $47.2 \pm 7.8 \text{ kJ mol}^{-1}$ .<sup>33</sup> However, the substantial differences in the setup (GDE versus full cell) limit the comparability. The settings for the optimization are summarized in Table S3.

### Conclusions

This study focuses on a detailed breakdown of ohmic and kinetic losses in a full cell PEMWE system. The ohmic resistance analysis reveals electronic resistances on the anode ( $14.1 \text{ m}\Omega \text{ cm}^2$ ) and cathode ( $22.7 \text{ m}\Omega \text{ cm}^2$ ), along with a temperature-dependent protonic resistance. Kinetic losses are further dissected into OER and HER components.

Utilizing a 3-electrode setup with temperature variation, the analysis includes key parameters such as the electronic resistances on the anode and cathode, the ratio between the swollen membrane thickness and the reference conductivity, the exchange current density at reference state and activation energy for half-cell reactions. The obtained values include  $\delta_{\text{mem}}/\kappa_0 = 7.7 \pm 0.4 \text{ m}\Omega \text{ cm}^2$ ,  $E_A^{\text{OER}} = 29.5 \pm 7.8 \text{ kJ mol}^{-1}$ ,  $i_{0,\infty}^{\text{OER}} = 1.1 \pm 3 \text{ mA cm}^{-2}$ , and  $E_A^{\text{HER}} = 9.9 \pm 1.2 \text{ kJ mol}^{-1}$ ,  $i_{0,\infty}^{\text{HER}} = 11.1 \pm 0.6 \text{ A cm}^{-2}$ .

This detailed analysis became possible through an improved experimental setup, featuring minimized impregnation impact, EIS for half-cells, and consideration of concentration potential. The impregnation volume for the PTL material in this study is found to be  $1 \mu\text{l}$  of 5 wt% Nafion™ solution. The results showcase the potential of the reference electrode setup, opening avenues for various research needs, including catalyst layer and porous transport layer material improvement.









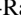
Future research directions could explore the full frequency range in EIS for comprehensive half-cell kinetics analysis. Additionally, the breakdown of ohmic resistance provides insights for addressing contact resistances between PTLs, with future enhancements possibly involving microporous layers and thin catalyst layers. This work provides a foundation for further exploration and refinement in PEMWE technology.

### Acknowledgments

The authors gratefully acknowledge the financial support by the Federal Ministry of Economic Affairs and Climate Action of Germany in the framework of HoKaWe (03EI3029B). The authors also thank Torben Gottschalk, Institute of Electric Power Systems LUH, for support in test station maintenance. Lena V. Böhre: Conceptualization, Methodology, Formal analysis, Investigation, Writing—Original Draft. Mustafa Murali: Formal analysis, Investigation (Impregnation study). Patrick Trinke: Supervision, Writing—review & editing. Jonathan Brandt: Formal analysis (Optimization, curve fitting), Writing—review & editing. Debora Brinkner: Investigation (EIS measurement for half-cells), Writing—review & editing. Gözde Kardes: Investigation (EIS

measurement for half-cells), Writing—review & editing. André Weber: Supervision (EIS measurement for half-cells), Writing—review & editing. Boris Bensmann: Supervision, Writing—review & editing, Project administration. Richard Hanke-Rauschenbach: Supervision, Writing—review & editing.

### ORCID

Lena V. Böhre  <https://orcid.org/0000-0002-8555-703X>  
 Mustafa Murali  <https://orcid.org/0009-0009-3111-6982>  
 Patrick Trinke  <https://orcid.org/0000-0002-0935-5321>  
 Jonathan Brandt  <https://orcid.org/0009-0003-5111-2352>  
 Debora Brinkner  <https://orcid.org/0009-0000-8033-5641>  
 Gözde Kardeş  <https://orcid.org/0000-0002-4213-7983>  
 André Weber  <https://orcid.org/0000-0003-1744-3732>  
 Boris Bensmann  <https://orcid.org/0000-0001-8685-7192>  
 Richard Hanke-Rauschenbach  <https://orcid.org/0000-0002-1958-307X>

### References

1. K. Ayers, N. Danilovic, R. Ouimet, M. Carmo, B. Pivovar, and M. Bornstein, *Annual Review of Chemical and Biomolecular Engineering*, **10**, 219 (2019).
2. B. S. Pivovar, M. F. Ruth, D. J. Myers, and H. N. Dinh, *Electrochem. Soc. Interface*, **30**, 61 (2021).
3. Q. Wu, Y. Wang, K. Zhang, Z. Xie, K. Sun, W. An, X. Liang, and X. Zou, *Mater. Chem. Front.*, **7**, 1025 (2023).
4. U. Babic, M. Suermann, F. N. Büchi, L. Gubler, and T. J. Schmidt, *J. Electrochem. Soc.*, **164**, F387 (2017).
5. K. C. Neyerlin, W. Gu, J. Jorne, and H. A. Gasteiger, *J. Electrochem. Soc.*, **153**, A1955 (2006).
6. L. V. Böhre, B. Bensmann, and R. Hanke-Rauschenbach, *J. Electrochem. Soc.* (2024), (JES-111849 (accept)).
7. A. Hartig-Weiß, M. Bernt, A. Siebel, and H. A. Gasteiger, *J. Electrochem. Soc.*, **168**, 114511 (2021).
8. L. V. Böhre, A. J. McLeod, P. Trinke, B. Bensmann, M. Benecke, O. E. Herrera, W. Merida, and R. Hanke-Rauschenbach, *J. Electrochem. Soc.*, **170**, 94507 (2023).
9. A. J. McLeod, L. V. Böhre, B. Bensmann, O. E. Herrera, and W. Mérida, *J. Power Sources*, **589**, 233750 (2024).
10. E. Brightman, J. Dodwell, N. van Dijk, and G. Hinds, *Electrochem. Commun.*, **52**, 1 (2015).
11. L. V. Böhre, S. Bullerdiek, P. Trinke, B. Bensmann, A.-L. Deutsch, P. Behrens, and R. Hanke-Rauschenbach, *J. Electrochem. Soc.*, **169**, 124513 (2022).
12. T. Schuler, T. J. Schmidt, and F. N. Büchi, *J. Electrochem. Soc.*, **166**, F555 (2019).
13. E. Padgett, G. Bender, A. Haug, K. Lewinski, F. Sun, H. Yu, D. A. Cullen, A. J. Steinbach, and S. M. Alia, *J. Electrochem. Soc.*, **170**, 084512 (2023).
14. R. B. Belsler and W. H. Hicklin, *J. Appl. Phys.*, **30**, 313 (1959).
15. H. Ito, T. Maeda, A. Nakano, and H. Takenaka, *Int. J. Hydrogen Energy*, **36**, 10527 (2011).
16. R. W. Kopitzke, C. A. Linkous, H. R. Anderson, and G. L. Nelson, *J. Electrochem. Soc.*, **147**, 1677 (2000).
17. R. García-Valverde, N. Espinosa, and A. Urbina, *Int. J. Hydrogen Energy*, **37**, 1927 (2012).
18. D. B. Spry and M. D. Fayer, *J. Phys. Chem. B*, **113**, 10210 (2009).
19. H. Becker, E. J.-F. Dickinson, X. Lu, U. Bexell, S. Proch, C. Moffatt, M. Stenström, G. Smith, and G. Hinds, *Energy Environ. Sci.*, **15**, 2508 (2022).
20. S. B. Adler, *J. Electrochem. Soc.*, **149**, E166 (2002).
21. M. Ender, J. Illig, and E. Ivers-Tiffée, *J. Electrochem. Soc.*, **164**, A71 (2017).
22. M. Ender, A. Weber, and I.-T. Ellen, *J. Electrochem. Soc.*, **159**, A128 (2011).
23. B. A. Boukamp, *J. Electrochem. Soc.*, **142**, 1885 (1995).
24. M. Schönleber and E. Ivers-Tiffée, *Electrochem. Commun.*, **58**, 15 (2015).
25. M. Schönleber, D. Klotz, and E. Ivers-Tiffée, *Electrochim. Acta*, **131**, 20 (2014).
26. MathWorks, *Equation Solving Algorithms*, **131**, 20 (2014), <https://de.mathworks.com/help/optim/ug/equation-solving-algorithms.html>.
27. S. Spelthann et al., *Optical Fibers and Sensors for Medical Diagnostics, Treatment, and Environmental Applications XXIV, SPIE Photonics West BiOS*, San Francisco, California 13 March 2024(SPIE)Proceedings Volume PC12835.8 (2024), Nanothermometers on fiber probe for in operando temperature measurements in water electrolysis cells <https://www.spiedigitallibrary.org/conference-proceedings-of-spie/PC12835/3001565/Nanothermometers-on-fiber-probe-for-in-operando-temperature-measurements-in/10.1117/12.3001565.short>.
28. M. Suermann, T. J. Schmidt, and F. N. Büchi, *Electrochim. Acta*, **281**, 466 (2018).
29. M. Kroschel, A. Bonakdarpour, J. T.-H. Kwan, P. Strasser, and D. P. Wilkinson, *Electrochim. Acta*, **317**, 722 (2019).
30. P. Lettenmeier, L. Wang, U. Golla-Schindler, P. Gazdzicki, N. A. Cañas, M. Handl, R. Hiesgen, S. S. Hosseiny, A. S. Gago, and K. A. Friedrich, *Angewandte Chemie (International ed. in English)*, **55**, 742 (2016).
31. M. Geuß et al., *J. Electrochem. Soc.*, **170**, 114510 (2023).
32. T. Schuler, T. Kimura, T. J. Schmidt, and F. N. Büchi, *Energy Environ. Sci.*, **13**, 2153 (2020).
33. A. R. Zeradjanin, P. Narangoda, J. Masa, and R. Schlögl, *ACS Catal.*, **12**, 11597 (2022).